Journal of Materials Chemistry A

ROYAL SOCIETY OF CHEMISTRY

PAPER

View Article Online
View Journal | View Issue



Cite this: J. Mater. Chem. A, 2025, 13, 15128

# Resonant defect states of the $SnO_2$:Ta transparent conductive oxide revealed by excitation wavelength-dependent Raman spectroscopy and hybrid functional DFT calculations†

Matthias Krause, *[a] Carlos Romero-Muñiz, [b] Oleksandr Selyshchev,[c] Dietrich R. T. Zahn [c] and Ramon Escobar-Galindo [d]

Excitation wavelength-dependent Raman spectroscopy, optical spectroscopy, and density functional theory (DFT) calculations with hybrid functionals were used to analyse the electronic structure of defects in $SnO_2$:Ta (1.25 at% Ta) transparent conductive oxide thin films. Based on the Raman excitation profiles of the characteristic $D_1$ and $D_2$ defect modes of two tin vacancy $V_{Sn}$-type defects and one oxygen interstitial $O_i$-type defect, we derived the corresponding defect-induced electronic transitions of the involved defect states. DFT calculations revealed additional density-of-states for the three point defects at the top of the valence band (VB) in comparison to defect-free $SnO_2$ and $SnO_2$:Ta. The largest distortion of the VB electronic structure was caused by the $V_{Sn}$-type defect with the farthest possible distance from the Ta dopant in the studied 96-atom supercell, and the smallest distortion was caused by the $O_i$-type defect. Accordingly, the amount of VB splitting showed a reverse order to the electronic transition energies. From the projected defect-density-of-states, we found a delocalized nature of the $V_{Sn}$-type defects and a localized nature of the $O_i$-type defect, accounting for the different degrees of distortion of the $SnO_2$:Ta electronic structure. Based on these complementary experimental and theoretical results, the electronic structure of point defects in the $SnO_2$:Ta transparent conductive oxide was elucidated in detail. Thus, the proposed approach has great potential to resolve the ongoing controversy about point defects in $SnO_2$.

Received 6th December 2024
Accepted 31st March 2025

DOI: 10.1039/d4ta08693g

rsc.li/materials-a



## 1 Introduction

Tin dioxide ($SnO_2$), indium oxide ($In_2O_3$) and zinc oxide (ZnO) belong to the family of classical transparent conductive oxides (TCOs).[1–6] In recent years, the research on $SnO_2$ as a TCO has focused on Ta-doped $SnO_2$ (TTO) because of its highly competitive resistivity and charge carrier mobility[7,8] and high chemical and thermal stabilities in high vacuum and in air.[9–11] The lowest resistivity of $1.1 \times 10^{-4}$ Ω cm and the highest mobility of 130 $cm^2 V^{-1} s^{-1}$ for $SnO_2$:Ta were obtained for TTO films prepared *via* pulsed laser deposition (PLD).[7,8] These values are only slightly worse than those of the best $In_2O_3$-based TCO films, with the resistivity values ranging from 6.7 to $8.6 \times 10^{-5}$ Ω cm and a mobility value of 250 $cm^2 V^{-1} s^{-1}$ for optimized Mo- and Sn-dopant concentrations.[12,13] The best electrical properties for magnetron sputtered $SnO_2$:Ta thin films were obtained by Weidner *et al.* with a resistivity of $5.4 \times 10^{-4}$ Ω cm and a mobility of 25.7 $cm^2 V^{-1} s^{-1}$.[14] Using spray pyrolysis deposition, Ramarajan *et al.* reported a resistivity of $4.36 \times 10^{-4}$ Ω cm.[15] A high mobility for TTO films of 23 $cm^2 V^{-1} s^{-1}$ was also achieved *via* sol–gel spin coating.[16] The electrical properties of TTO thin films surpass those of $SnO_2$:F (FTO) and $SnO_2$:Sb (ATO), the lowest resistivities of which were $5 \times 10^{-4}$ Ω cm and of the order of $10^{-3}$ Ω cm, respectively.[14,17–21]

Point defects, including substitutional dopants, are crucial for the electrical, optical and chemical properties of TCOs. For a long time, oxygen vacancies ($V_O$) were considered to be responsible for the low intrinsic resistivity of undoped and mostly slightly oxygen-deficit $SnO_2$.[5,22,23] More recently, tin interstitials, $Sn_i$,[24] [$V_O$ + $Sn_i$] complexes,[24] or substitutional hydrogen[25] were proposed as the main n-type donors in non-intentionally doped $SnO_2$ based on local-density approximation (LDA) and generalized gradient approximation (GGA) DFT

[a]Institute of Ion Beam Physics and Materials Research, Helmholtz-Zentrum Dresden-Rossendorf, Bautzner Landstraße 400, 01328 Dresden, Germany. E-mail: matthias.krause@hzdr.de

[b]Departamento de Física de la Materia Condensada, Universidad de Sevilla, PO Box 1065, 41080 Sevilla, Spain

[c]Institute of Physics, Technische Universität Chemnitz, Reichenhainer Straße 70, 09126 Chemnitz, Germany

[d]Departamento de Fisica Aplicada I, Escuela Politécnica Superior, Universidad de Sevilla, 41011 Seville, Spain

† Electronic supplementary information (ESI) available. See DOI: https://doi.org/10.1039/d4ta08693g

calculations. Additionally, using the GGA-DFT level of theory, Godinho *et al.* proposed a defect cluster comprised of $V_O^{\cdot\cdot}$ and $Sn_i''$ as the most stable defect in $SnO_{2-x}$, *i.e.*, a complex comprised of a neutral oxygen vacancy and an interstitial $Sn^{2+}$ ion next to it.[26] In the case of $SnO_2$ with excess oxygen, their calculations predicted the formation of an interstitial peroxide molecule ion ($O_2^{2-}$) as the most stable point defect. Most recent hybrid functional DFT calculations again indicated that $V_O$-type defects are the most stable defects in undoped Sn-rich $SnO_{2-x}$.[27] Under O-rich conditions, the $O_i$-type defect was found to be the most stable point defect for a broad range of defect charge states, without specifying it as being either single-atomic or molecular nature.[27]

In the case of Ta-doped $SnO_2$, DFT calculations at different levels of theory (Table 1) agree that substitutional Ta, $Ta_{Sn}$, is a point defect with a very low formation energy. When different point defects were considered, $Ta_{Sn}$ was always predicted to be the easiest formed defect, independently of whether the samples are O-rich or O-poor.[10,27–29] The superior electrical properties achieved for TTO in comparison to ATO or FTO were attributed to the so-called resonant doping, which is characterized by non-hybridizing Ta 5d donor states situated 1–2 eV above the conduction band minimum, first proposed by Williamson *et al.* in 2020.[16,29,30] Regarding the other point defects of TTO, the theoretical data are less consistent, and also not complete. Williamson *et al.*[29] and our group[10] found an increased formation energy for the $V_O$-type defect compared to undoped $SnO_2$, which was not confirmed by Wang *et al.*[27] The $O_i$-type defect was predicted as the second-stable defect for O-rich compositions by two groups.[10,27] Although this point defect was further specified to be comprised of a peroxide ion in ref. 10, this information is missing in ref. 27. The $V_{Sn}$-type defect was predicted to have a very high formation energy under O-poor conditions,[27] but to be stabilized by an excess of oxygen[27] and the presence of substitutional Ta.[10] Filippatos *et al.* focused on the bandgap and density of states of only two point defects in $SnO_2$:Ta, namely substitutional $Ta_{Sn}$- and interstitial $Ta_i$-type defects.[30]

The partially controversial and incomplete results described above underline the necessity for the verification of the most relevant point defects in $SnO_2$-based TCOs, ideally combining experimental and theoretical data. In a previous paper, we systematically studied the principal point defects in slightly O-rich $SnO_2$ and $SnO_2$:Ta (exp.: 1.25 at% Ta, calc.: 1.04 at% Ta) samples *via* a combined Raman spectroscopy and DFT study.[10] The characteristic and dominant Raman lines of $V_{Sn}$-type and $O_i$-type defects out of the $SnO_2$ phonon range, labelled by $D_1$ and $D_2$, respectively, were identified. This study supported the formation of peroxide ions as $O_i$-type defects for O-rich $SnO_2$ predicted before.[26]

Due to the dominance of the two defect lines $D_1$ and $D_2$, the Raman spectra of Ta-doped $SnO_2$ differed essentially from that of undoped, rutile-type $SnO_2$ crystals, thin films, nanowires and nanoparticles.[31–36] The reason for the dominance of the defect modes in the Raman spectra of TTO in comparison to the $SnO_2$ lattice modes is still not clear. Moreover, the effect of the corresponding defects on the electronic structure of $SnO_2$:Ta is not understood. This means that it is unclear whether the two defect types, $V_{Sn}$ and $O_i$, are favourable or unfavourable for the electrical and optical properties of $SnO_2$:Ta. In a more general context, the unambiguous identification of point defects in TCOs remains a challenging task but can substantially support the optimization of the electric and optical properties of these materials. Therefore, the aim of this work was to show that the combination of excitation wavelength-dependent Raman spectroscopy, optical spectroscopy, and DFT calculations using hybrid functionals can reveal the electronic structure of the transparent conductive oxide $SnO_2$:Ta, including that of the various point defects.

Excitation wavelength-dependent Raman spectra of TTO thin films were measured using eight laser lines in the range of 785 nm (NIR) to 325 nm (UV), or in energy units, 1.58 eV to 3.81 eV. The Raman excitation profiles were obtained by plotting the intensity of the most relevant lattice and defect modes against the laser wavelength. The maxima of these profiles correspond to electronic transition energies. The principal optical band gap of the studied material was determined by optical spectroscopy. Hybrid functional DFT calculations of the electronic structure of 96-atom supercells of $SnO_2$ and $SnO_2$:Ta (1.04 at% Ta) were applied to identify the effects of Ta substitution and $V_{Sn}$- and $O_i$-type defects on the electronic band structure, with a focus on the density of states close to the valence band maximum (VBM) and the conduction band minimum (CBM). Based on complementary experimental and theoretical results, detailed insight in the electronic structure of the $SnO_2$:Ta transparent conductive oxide could be achieved, including the energetic order and localized/delocalized nature of the different point defects.

Table 1 Comparison of the levels of theory, supercell sizes, Ta concentrations, and applied stopping criteria in previous DFT calculations on $SnO_2$:Ta. HSE: Heyd–Scuseria–Ernzerhof hybrid functional; PBE: Perdew–Burke–Ernzerhof functional; and GGA: generalized gradient approximation

| | | | | Convergence criteria | |
|---|---|---|---|---|---|
| Reference | DFT level | Supercell size | Ta conc./at% | eV Å$^{-1}$ | eV |
| Behtash *et al.*[28] | HSE | 2 × 2 × 3 | 1/72 = 1.4 | 0.01 | $10^{-4}$ |
| Williamson *et al.*[29] | PBE0 (hybrid) | 2 × 2 × 3 | 1/72 = 1.4 | 0.01 | n.a. |
| Krause *et al.*[10] | PBE | 2 × 2 × 4 | 1/96 = 1.04 | 0.005 | $10^{-6}$ |
| Filippatos *et al.*[30] | PBE0 (hybrid) | 2 × 2 × 2 | 1/48 = 2.1 | 0.05 | $2 \times 10^{-5}$ |
| Wang *et al.*[27] | GGA, HSE06 | 3 × 3 × 5 | 1/270 = 0.4 | 0.01 | $10^{-5}$ |

# 2 Experimental and theoretical methodology

## 2.1 Excitation wavelength-dependent Raman analysis of $SnO_2$:Ta (1.25 at% Ta)

Eight laser lines in the near-infrared (785 nm) to the UV (325 nm) spectral range were used to measure the Raman spectra of a Ta-doped $SnO_2$ (1.25 at% Ta). The studied sample had a thickness of approx. 1.6 μm and was grown by reactive direct current magnetron sputtering on fused silica. The experimental details for the sample fabrication were described and published previously.[9,10,37,38] The Ta-concentration of 1.25 at% was chosen given that it yielded the best electrical properties based on the dependence of the specific resistivity, carrier mobility, and the carrier concentration on the Ta concentration studied in detail in ref. 9. The full element composition as determined by Rutherford backscattering spectrometry and elastic recoil detection analysis was 1.25 at% Ta, 31.9 at% Sn, and 66.9 at% O.[10] This composition was homogeneous for the entire film thickness. For the micro-Raman measurements at room temperature, four spectrometers (Horiba) located at HZDR and at TU Chemnitz were employed. All were equipped with either thermoelectric (TE) or liquid $N_2$ ($LN_2$) cooled CCD detectors. The other spectrometer parameters are presented in Table 2.

The laser radiation was focused to a spot of approx. 1 μm diameter at the sample surface by 100-fold magnifying long-working-distance objectives. In the UV experiment, a $CaF_2$ near-UV objective with 40-fold magnification was used. Typically, Raman spectra were measured from three different sample positions and averaged for the spectrum fit analysis. To obtain the Raman excitation profiles, for each laser wavelength the individual line intensities (arb. un.) were divided by the overall scattering intensity (arb. un.) in the wavenumber range of 350 to 950 $cm^{-1}$, resulting in the relative intensity in (%) units.

## 2.2 Optical characterization of $SnO_2$:Ta (1.25 at% Ta)

For the optical characterization, a TTO sample on fused silica of approx. 0.3 μm thickness was used to reduce the effect of the transmission drop at short wavelengths. The transmittance ($T$) and specular reflectance ($R$) of the sample were measured using a SolidSpec 3700 DUV spectrometer (Shimadzu). The experimental parameters were a spectral resolution of 5 nm, a step width of 2 nm, and a scanning speed of approx. 280 nm $min^{-1}$. The reflectance was measured under an incidence angle of 5° relative to the surface normal. The absorbance ($A$) of the sample was calculated using the relation for energy conservation, $A = 1 - R - T$. A Tauc-plot type analysis for crystalline samples was used for the estimation of the optical gap of $SnO_2$:Ta (1.25 at% Ta), following the relation $\alpha h\nu \approx (h\nu - E_{gap})^r$.[39,40] Therefore, the expression $(\alpha h\nu)^{1/r}$ ($\alpha$: absorption coefficient, $r = 0.5$ for dipole-allowed optical transitions) was plotted as a function of the photon energy. The linear range of the plot was fitted by a linear function and the optical band gap was estimated from its intercept with the energy axis.

## 2.3 Hybrid functional DFT calculations

In our previous work,[10] we used standard DFT calculations to study the structural and vibrational properties of $SnO_2$ and the influence of several point defects (Table 1 in ref. 10). Our current approach is essentially the same but using a hybrid functional, namely, the HSE06 functional[41] (HSE: Heyd–Scuseria–Ernzerhof hybrid functional) as implemented in the VASP package.[42] For each defective system, we performed a single-point calculation to obtain the density of states (DOS) of the system with the hybrid functional, using a Monkhorst–Pack grid of $2 \times 2 \times 2$ in the 96-atom cells that we described in our previous work.[10]

It is well-known that standard DFT (*i.e.*, DFT based on LDA or GGA) can properly predict the experimental values of the lattice constants and atomic positions of most chemical compounds including oxides such as $SnO_2$. However, they fail when describing the electronic properties of insulators, especially their band gaps.[43,44] For this purpose, the use of hybrid functionals such as HSE06 is entirely necessary.[41] It is worth noting that in 2010, J. B. Varley and coworkers showed that the use of a higher fraction of exact Hartree–Fock exchange contribution (33%) to the HSE hybrid functionals leads to an almost perfect match of the experimental band gap of $SnO_2$.[45] This fact was confirmed by subsequent studies.[27,28] However, the optimization of the mixing parameter is a purely empirical result based exclusively on the band gap tuning of bulk $SnO_2$. Thus, it might not work well for defective systems, and moreover there is no guarantee that they accurately reproduce other aspects of the

Table 2 Laser lines, spectrometer type, grating, spectral resolution, and detector used for excitation wavelength-dependent Raman measurements of $SnO_2$:Ta (1.25 at% Ta). BIDD: back-illuminated deep-depleted, EM: electron-multiplying

| Laser line/nm | Spectrometer type | Grating 1/mm | Resolution/$cm^{-1}$ | CCD type |
|---|---|---|---|---|
| 325 | LabRam HR | 2400 | 3.2 | BIDD-TE |
| 405 | LabRam Evolution | 1800 | 3.0 | BIDD-$LN_2$ |
| 473 | iHR 550 | 1800 | 3.0 | BIDD-$LN_2$ |
| 488 | LabRam HR | 2400 | 1.5 | BIDD-TE |
| 514.7 | LabRam HR | 2400 | 1.3 | BIDD-TE |
| 532 | LabRam Evolution | 1800 | 1.5 | BIDD-$LN_2$ |
| | iHR 550 | 1800 | 2.0 | BIDD-$LN_2$ |
| 633 | LabRam Evolution | 1800 | 1.0 | BIDD-$LN_2$ |
| 785 | XPlora | 1200 | 2.0 | EM-TE |

 

electronic structure not related to the band gap. Consequently, we used the HSE06 hybrid functional in its standard form with 25% of exact Hartree–Fock exchange contribution.

# 3 Results

## 3.1 Laser-wavelength dependence of the Raman spectra of $SnO_2$:Ta (1.25 at% Ta)

When Raman scattering of $SnO_2$:Ta (1.25 at% Ta) is excited with eight different laser wavelengths from 785 to 325 nm, distinct differences of the relative line intensities are observed (Fig. 1). The most obvious one was the transition from the $D_1$ defect-line-dominated spectral structure in the visible spectral range (633 nm to 405 nm) to an $L_4$ and $L_5$ lattice-mode-dominated structure when UV laser radiation was applied. The $L_4$ and $L_5$ lattice modes were derived from the $A_{1g}$ mode of crystalline undoped $SnO_2$.[31,32] The relative intensities of these two Raman lines in the spectra measured with 785 nm laser excitation are also higher than in those excited with visible lasers. Different to the response in the UV, for NIR excitation, the $L_4$ line was stronger than the $L_5$ line. The second defect-induced Raman line $D_2$ has an apparent intensity maximum for excitation with the deep blue laser line of 405 nm. In the following analysis, we focus on these four selected lines. The colour code of the Raman line labels below the spectra in Fig. 1 provides a rough guideline for the laser wavelength that the most prominent Raman lines have their apparent intensity maximum.

Prior to the detailed analysis of the intensity evolution as a function of the excitation wavelength for the $D_1$ and $D_2$ defect lines and the $L_4$ and $L_5$ $A_{1g}$-derived lattice modes, a possible laser-wavelength-dependence of the line frequencies had to be checked. Such a dependence could have indicated the presence of different Raman lines, which are close in frequency but belong to different structures and are selectively enhanced for specific laser lines. The frequencies of three of the four relevant lines ($D_2$, $L_4$, and $L_5$) were immediately found to be independent of the laser wavelength within the experimental accuracy (Fig. 2). Because the fit errors are larger for the overlapping $L_4$ and $L_5$ lines, their total frequency error is larger than that of the $D_1$ and $D_2$ lines. In contrast to the three other selected lines, the $D_1$ line shows a significant shift, despite its very small frequency error (Fig. 2). A single Lorentzian fit model for the $D_1$ line resulted in a large residual intensity compared with the experimental data (SI 1†). A significantly better fit was achieved by a two Lorentzian model, indicating a splitting of the $D_1$ line into a low-energy ($D_1$-low) and a high-energy ($D_1$-high) component (SI 1†). Their mean frequencies are 402 ± 1 $cm^{-1}$ and 412 ± 1 $cm^{-1}$, respectively. Thus, both $D_1$-line components have frequencies that are independent of the laser wavelength. The $D_1$-high component has a higher intensity only for 325 nm and 405 nm laser excitation, accounting for the observed upshift in frequency under these conditions (Fig. 2).

Different $D_1$ line frequencies indicate different structural environments of the $V_{Sn}$ point defect. According to DFT calculations, a $D_1$ line position of 431 $cm^{-1}$ was found for the $V_{Sn}$-type defect located at the largest possible distance from the $Ta_{Sn}$ atom in the supercell ($SnO_2$:Ta-$V_{Sn}$-2 (far from Ta)), and a frequency of 434 $cm^{-1}$ was calculated for the model structure with directly neighbouring $V_{Sn}$ and $Ta_{Sn}$ ($SnO_2$:Ta-$V_{Sn}$-1 (near Ta)).[10] Although the experimentally determined difference

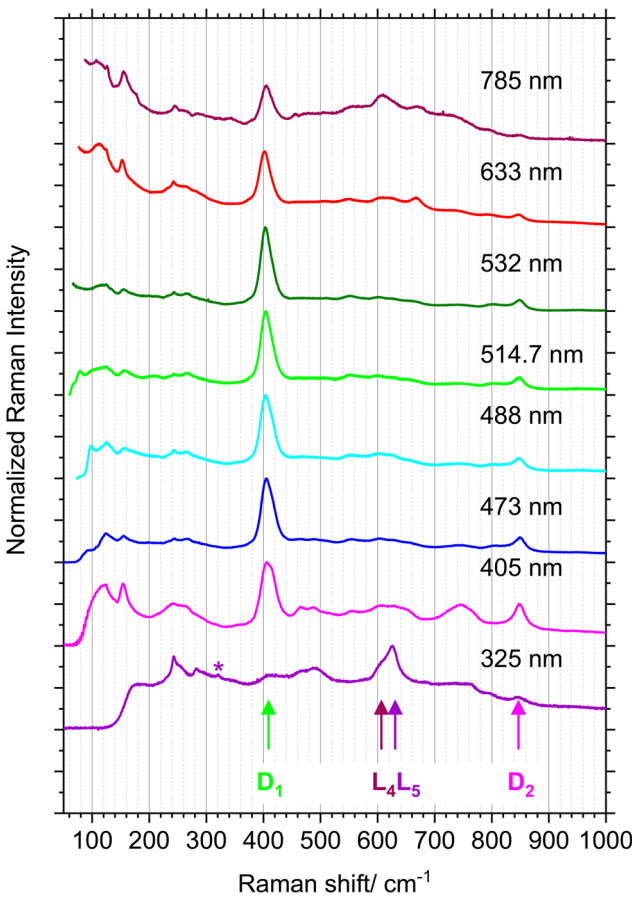


Fig. 1 Raman spectra of $SnO_2$:Ta (1.25 at% Ta) as a function of the excitation wavelength. The colour code of the line labels indicates the laser wavelength at which the most prominent lines have their apparent intensity maximum. The asterisk indicates a line caused by the $CaF_2$ microscope objective used for UV excitation.

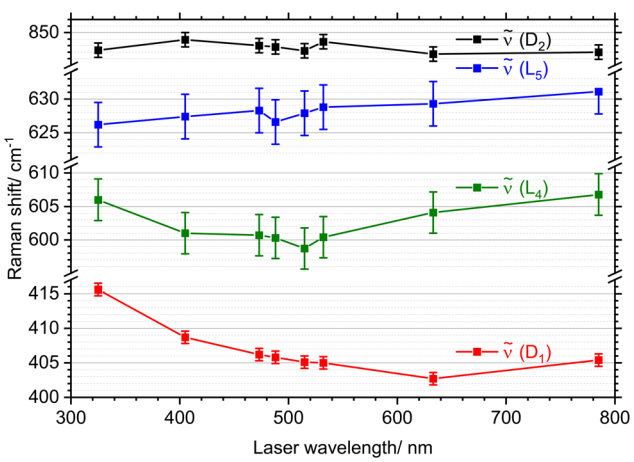


Fig. 2 Raman shifts of the most prominent Raman lines of $SnO_2$:Ta (1.25 at% Ta) as a function of the laser wavelength.

between the two $D_1$ line components is larger than that of the calculated frequencies of the two model structures, the qualitative agreement of both data sets supports the existence of different $V_{Sn}$ defect structures in the studied $SnO_2$:Ta (1.25 at% Ta) samples.

Given that the designation of the defect structures proposed in ref. 10 (see previous paragraph) seems too technical for the current paper, herein we simplify the termini to $SnO_2$:Ta-$V_{Sn}$-near and $SnO_2$:Ta-$V_{Sn}$-far, and in the same way for the $O_i$-type defect structures.

### 3.2 Excitation profiles of selected Raman lines of $SnO_2$:Ta (1.25 at% Ta)

The excitation wavelength-independent frequencies of the selected $SnO_2$:Ta Raman lines including $D_1$-low and $D_1$-high show that these lines always originate from the same vibrational modes. This allows the investigation of the dependence of their Raman intensity from the exciting laser wavelength and laser energy. Given that the Raman scattering intensity has resonance character, according to[46]

$$I(E_{\text{laser}}) \propto \left| \frac{A}{(E_{\text{laser}} - E_{\text{gap}} - i\gamma)(E_{\text{laser}} - (E_{\text{gap}} \pm E_{\text{q}}) - i\gamma)} \right|^2, \quad (1)$$

the Raman intensity of selected lines can be resonantly enhanced when the laser energy ($E_{\text{laser}}$) matches the energy of an electronic transition ($E_{\text{gap}}$) or the energy of the scattered light ($E_{\text{gap}} \pm E_{\text{q}}$; $E_{\text{q}}$ is the energy of the involved phonon) in the studied system. The damping term $i\gamma$ prevents an infinite increase of the Raman line intensities and the numerator $A$ includes the integral of the matrix elements of the Raman transition. Plotting the Raman line intensities against the laser wavelength gives the Raman excitation profiles, which allow conclusions about the electronic transitions of the studied samples.[47–54]

The Raman excitation profiles of the $D_1$-low and $D_1$-high lines can be well-described by single Gaussian profiles (Fig. 3). For example, a corrected $r^2$ of 0.985 was obtained for the fit of $D_1$-low with a Gaussian fit compared to 0.933 for the Lorentzian profile. The comparison of the integral intensities in the maximum and edge regions of the profiles yielded an enhancement by approx. a factor of 5 for both $D_1$ lines. Moreover, the excitation profile maxima of $D_1$-low and $D_1$-high are found at slightly different wavelengths, as seen in Fig. 3a, b, and Table 3. The data in Table 3 indicate that both excitation profile maxima do not overlap even if the error bars are considered. This finding supports the existence of two $V_{Sn}$-type defect structures in $SnO_2$:Ta (1.25 at% Ta). In addition to slightly different Raman frequencies, they have different electronic transition energies ($\Delta E$). The transition energy difference of 0.08 eV corresponds to approx. 3 times $kT$ for room temperature.

In the case of the $D_2$ defect line, the two Gaussian line fit provided a much better fit than the single Gaussian one (Fig. 3c and d), respectively. It resulted in a much smaller residual intensity and gave better corrected $r^2$ values. As expected from the evolution of the spectra as a function of the laser wavelength

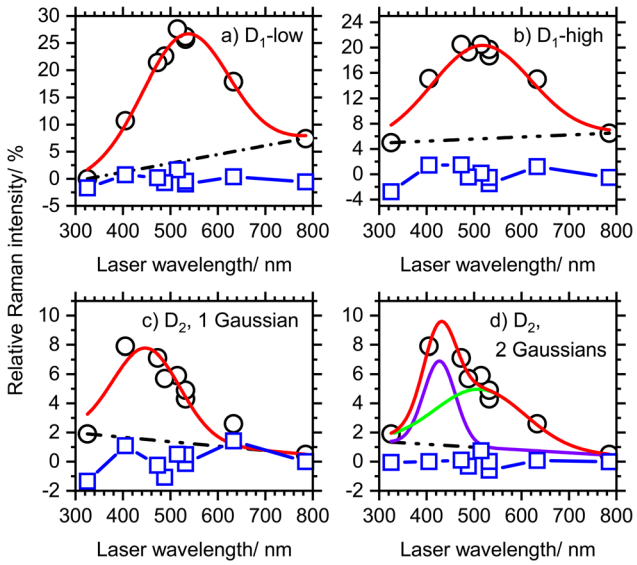


Fig. 3 Raman excitation profiles of the $V_{Sn}$-type and $O_i$-type lines of $SnO_2$:Ta (1.25 at% Ta). (a) $V_{Sn}$-type line $D_1$-low (corrected $r^2 = 0.985$), (b) $V_{Sn}$-type line $D_1$-high (corrected $r^2 = 0.923$), (c) $O_i$-type line $D_2$, 1 Gaussian peak (corrected $r^2 = 0.813$), and (d) $O_i$-type line $D_2$, 2 Gaussian peaks (corrected $r^2 = 0.916$). The blue coloured traces (connected squares) represent the regular residuals of the fits and the dash-dotted black lines represent the fitted baseline.

(Fig. 1), one resonance maximum of the $D_2$ Raman line is located in the deep blue spectral range at 427 nm or 2.90 eV (Table 3). However, according to the 2 Gaussian line fit, a second resonance maximum exists for green laser wavelengths. This $D_2$ line resonance maximum fits the resonance maximum of the $D_1$-high defect line (Table 3). It should be noted that the error of the second $D_2$ line excitation profile maximum is large. Thus, although its presence is justified by the asymmetric line shape of the excitation profile and the significantly better fit quality, this error leaves some uncertainty about the energy of this electronic transition. Independently, the analysis of the resonance Raman excitation profile maxima of $SnO_2$:Ta (1.25 at% Ta) demonstrated the occurrence of three defect-related electronic transitions ($\Delta E$) with the following energetic order:

$\Delta E_1$ ($D_2$ line) > $\Delta E_2$ ($D_1$-high + $D_2$ line) > $\Delta E_3$ ($D_1$-low line) (see Table 3).

The Raman excitation profiles of the $L_4$ and $L_5$ lattice modes cannot be described by spectral line functions (Fig. 4). Both the

Table 3 Wavelengths and corresponding electronic transition energies of the Raman excitation profile intensity maxima of the $D_1$-low, $D_1$-high, and $D_2$ Raman modes

| | | Excitation profile maximum | |
|---|---|---|---|
| Raman mode | Raman shift/cm$^{-1}$ | Wavelength/nm | Energy/eV |
| $D_1$-low | 402 ± 1 | 532 ± 5 | 2.33 ± 0.02 |
| $D_1$-high | 412 ± 1 | 515 ± 11 | 2.41 ± 0.05 |
| $D_2$ | 848 ± 1 | 513 ± 44 | 2.42 ± 0.22 |
| | | 427 ± 21 | 2.90 ± 0.15 |

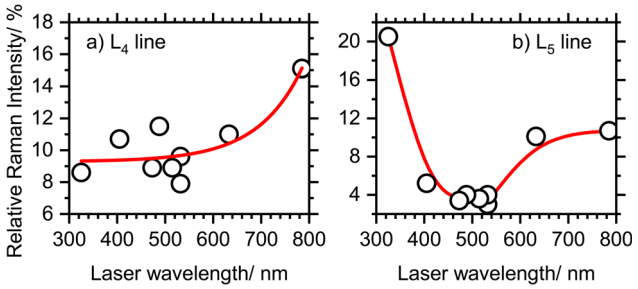


Fig. 4 Raman excitation profiles of the $A_{1g}$-derived Raman lines of $SnO_2$:Ta (1.25 at% Ta): (a) $L_4$ line and (b) $L_5$-line. The exponentially increasing fit function towards the NIR for (a) and the solid line for (b) are guides for the eye.

$L_4$ and $L_5$ $A_{1g}$-derived lines have low intensity when the $D_1$ and $D_2$ lines have their resonance maxima. The $L_4$ line intensity is almost independent of the laser wavelength, except for a slight increase by a factor of 1.5 for 785 nm excitation (Fig. 4a). The intensity evolution for the $L_5$ line is more complex. The data indicated an increase by a factor of 5 for UV excitation, which might be caused by the pre-resonance enhancement related to the principal band gap transition of $SnO_2$:Ta. Moreover, $L_5$ displays a moderately higher intensity (by approx. a factor of 2.5) for the red and NIR laser lines compared to excitation by blue and green light (Fig. 4b).

### 3.3 Analysis of the optical spectra of $SnO_2$:Ta (1.25 at% Ta)

It is now interesting to relate the transition energies of the defect states to the optical bandgap of the studied TTO. The generally accepted bandgap of intrinsic $SnO_2$ is 3.6 eV or slightly higher.[5,6,29] Substitutional n-type doping usually results in partial filling of the conduction band, which increases the effective band gap in comparison to pristine $SnO_2$. The optical spectra of $SnO_2$:Ta (1.25 at% Ta) exhibit a sharp increase of the absorbance in the UV range, starting at approx. 300 nm (Fig. 5a). Two minor maxima at approx. 410 nm (3.0 eV) and 590 nm (2.1 eV; Fig. 5a) and a shoulder at approx. 325 nm (3.8 eV) in the absorption spectra are related to the interference pattern of the optically transparent thin film with a thickness of approx. 300 nm. The reflectivity edge in the NIR range is due to the plasma absorption of the free charge carriers. The Tauc-plot type analysis showed a linear relation between photon energy and $(\alpha h\nu)^2$ in the energy range of 4.25 eV to 4.475 eV. Such a correlation is characteristic for dipole-allowed, direct optical transitions of crystalline semiconductors.[55] Its intercept with the energy axis, $4.13 \pm 0.10$ eV, corresponds to the optical band gap of the studied $SnO_2$:Ta (1.25 at% Ta) (Fig. 5b). This value is in very good agreement with the findings of Williamson *et al.* and Uwihoreye *et al.*, who reported values of 3.98 eV to 4.13 eV and 4.20 eV to 4.24 eV, respectively.[16,29] The corresponding charge carrier concentrations were $1.8 \times 10^{20}$ to $6.3 \times 10^{20}$ $cm^{-3}$ and $1.13 \times 10^{20}$ to $2.33 \times 10^{20}$ $cm^{-3}$,[16,29] respectively, similar to that of the samples studied here ($2.0 \times 10^{20}$ $cm^{-3}$ to $4.6 \times 10^{20}$).[9,37,38]

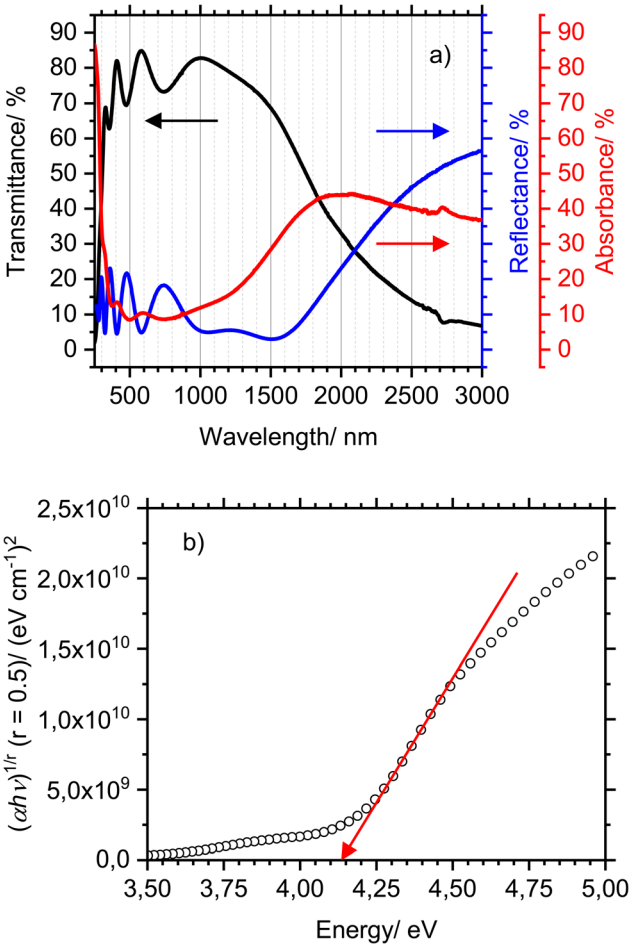


Fig. 5 Optical properties of $SnO_2$:Ta. (a) Measured transmittance and reflectance spectra and calculated absorbance spectrum. (b) Tauc-plot type analysis of the band gap of $SnO_2$:Ta. The corrected $r^2$ for the linear fit is 0.999 and fulfils the goodness of fit criterion of $r^2 > 0.99$ defined by Zanatta *et al.*[55]

The analysis of the optical spectra implies that the defect states revealed by the Raman excitation profiles are located within the band gap. Their nature and effects on the electronic structure of $SnO_2$:Ta are addressed in the following section.

### 3.4 Hybrid functional DFT calculations of the electronic structure of $SnO_2$:Ta (1.25 at% Ta)

To gain further insight into the electronic properties of our defective $SnO_2$ system, we performed DFT calculations using hybrid functionals, as described in Section 2.3. As a benchmark starting point, the DOS of pure $SnO_2$ was calculated in agreement with previous work using similar methodologies.[27,28,30] The valence band (VB) is dominated by O 2p states, which give rise to a strong doublet-shaped DOS maximum at its high-energy edge (Fig. 6a, SI 2 and SI 4†). Minor contributions are derived from the Sn 4d states (close to the VBM) and Sn 5s states (approx. 7 eV below the VBM, SI 2†). The conduction band (CB) is predominantly derived from the Sn 5s states (SI 2†). Its bottom edge is not well defined due to the presence of weak peaks, representing states with a very low density. Substituting

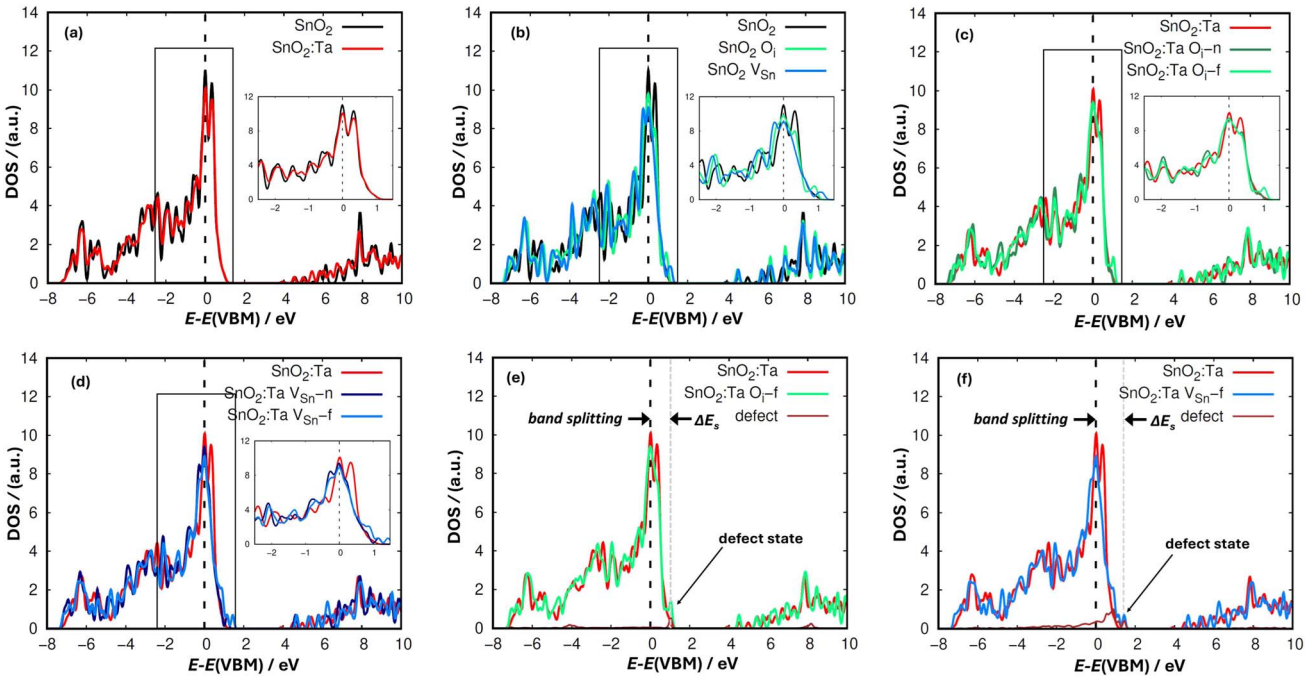


Fig. 6 Calculated DOS of $SnO_2$, $SnO_2$:Ta and some defective systems in a 96-atom supercell leading to Ta concentrations of approx. 1 at%. (a) Comparison between pure $SnO_2$ (black line) and $SnO_2$:Ta (red line). (b) Comparison between pure $SnO_2$ and $SnO_2$ with point defects: $SnO_2$-$O_i$ (green line) and $SnO_2$-$V_{Sn}$ (blue line). (c) Comparison between $SnO_2$:Ta and $O_i$ defective systems (green lines) located at different distances of the Ta atom. (d) Comparison between $SnO_2$:Ta and $V_{Sn}$ defective systems (blue lines) located at different distances of the Ta atom. (e) Projection of the $O_i$-far defect states in the DOS of the model structure $SnO_2$:Ta-$O_i$-far (brown line). (f) Projection of the $V_{Sn}$-far defect states in the DOS of the model structure $SnO_2$:Ta-$V_{Sn}$-far (brown line).

one Sn by one Ta atom ($Ta_{Sn}$) leaves the high-energy VB states almost unchanged. The characteristic O 2p doublet structure as well as the signatures of the minor Sn contributions are conserved (SI 2†). The Ta contribution in this energy range is very small (Fig. 6a and SI 2†). The most significant changes occur in the CB. A Ta 5d state is found approx. 1 eV above the empty Sn 5s states at the CBM (Fig. 6a, SI 2 and SI 4†). This state could be responsible for a spontaneous (resonant) net charge transfer to the Sn 5s CB, as proposed by Williamson *et al.*[29] Moreover, the substitutional Ta atom causes a slight downshift in the bottom CB Sn 5s states and is responsible for the additional Ta 5d states at approx. 2 eV above the CBM (Fig. SI 2 and SI 4†).

Now, we focus on the point defects responsible for the defect-induced Raman signatures observed in our experiments. That is, interstitial oxygen atoms ($O_i$) and tin vacancies ($V_{Sn}$). Fig. 6b and SI 4b† show the impact of these defects on the DOS of undoped $SnO_2$. For both types of defects, the VB broadens and satellite DOS peaks emerge at the top of the VB, giving rise to a VB splitting. Broadening and splitting are more pronounced for the Sn vacancy defects (>1.0 eV above zero energy reference, see also Table 4). The energy of the VB maximum DOS is used as the zero energy reference. The detailed analysis of these contributions revealed that they indeed arise from the point defects. The corresponding $O_i$ states are localized in the interstitial peroxide ions, and for $V_{Sn}$ these states appear on the four closest O atoms near the tin vacancy (see Fig. SI 3b and d,† respectively). Table 4 provides a detailed comparison of the VB splitting in all the defective systems considered in this work. The DOS at the bottom of the CB also changed compared to the defect-free $SnO_2$ and $SnO_2$:Ta. In these cases, the bottom edge of the CB-DOS is clearly defined at variance with the free-defect systems (see inset in Fig. 6b and SI 4†).

Fig. 6c, SI 3a and SI 4c† show the impact of $O_i$ defects on the Ta-doped $SnO_2$ system. The VB splitting of $SnO_2$:Ta-$O_i$-far is larger, and that of $SnO_2$:Ta-$O_i$-near is as large as that for $SnO_2$-$O_i$ (Table 4). The DOS structure of the CB is in good approximation not affected by the position of the $O_i$ defect relative to the Ta dopant atom (Fig. SI 4c†). Fig. 6d and SI 4† show the effect of $V_{Sn}$ defects in the $SnO_2$:Ta system. Among the model structures considered in this study, $SnO_2$:Ta-$V_{Sn}$-far showed the largest VB splitting. A fine structure comprising several shoulders or local

Table 4 Valence band splitting found in defective systems of $SnO_2$ and $SnO_2$:Ta relative to the zero reference level

| System | Valence band splitting ($\Delta E_s$)/eV |
|---|---|
| $SnO_2$-$O_i$ | 0.91 |
| $SnO_2$:Ta-$O_i$ (near) | 0.90 |
| $SnO_2$:Ta-$O_i$ (far) | 1.03 |
| $SnO_2$-$V_{Sn}$ | 1.11 |
| $SnO_2$:Ta-$V_{Sn}$ (near) | 1.16 |
| $SnO_2$:Ta-$V_{Sn}$ (far) | 1.44 |

maxima can be verified in the DOS of the high-energy VB edge. The highest VB-DOS is located 1.44 eV above the zero reference level, which is 0.28 eV higher than the highest VB-DOS of $SnO_2$:Ta-$V_{Sn}$-near (Table 4). The CBM level of this model structure is also slightly higher in energy than that of $SnO_2$:Ta-$V_{Sn}$-near. The different extents of splitting of the VB states imply that the largest distortion of the VB electronic structure of $SnO_2$:Ta is caused by the $V_{Sn}$-type defect with the farthest possible distance from the Ta dopant in the studied 96-atom supercell, followed by the $V_{Sn}$-near defect, and the smallest one by the $O_i$-type defect. The order of the VB splitting is inverse to the order of the electronic transition energies revealed by the resonance Raman excitation profiles. Consistently, a high electronic transition energy corresponds to a small VB splitting and *vice versa*.

A possible reason for the observed behaviour is found in the projected partial DOS of the defects (Fig. 6e and f). The $O_i$-far-type defect is characterized by narrow peaks in the density of states, which indicate the discrete and localized nature of this defect. This is in agreement with its origin of a peroxide molecule ion ($O_2^{2-}$),[10] which is electronically de-coupled from the rest of the band structure. Fig. 6f shows the projected density of states of the four oxygen atoms near the $V_{Sn}$-far type defect. In contrast to the former case, this defect has a broad energy distribution at the high-energy VB edge (Fig. 6f), which indicates its delocalized nature and strong coupling with the electronic system of the $SnO_2$:Ta host.

We did not detect a noticeable difference in the band gap between the pure $SnO_2$ and $SnO_2$:Ta systems and the defective systems. Apparently, this result seems to contradict the so-called Burstein–Moss effect. In principle, partial filling of the CB by free carriers of the dopants should lead to an increment in the optical band gap, observed in our experiments. However, a naïve evaluation of the Burstein–Moss shift by comparing the DOS of the undoped and doped $SnO_2$ systems might not be appropriate. This is because the experimental optical absorption shift also depends on other factors not visible from the electronic structure. Some authors pointed out that the difference between the edge of the CB and the VBM may account for the optical band gap instead of the purely electronic band gap.[28,56] However, this is only a rough estimation in the best scenario.

# 4 Discussion

## 4.1 New insights for the interpretation of the Raman spectra of $SnO_2$:Ta (1.25 at% Ta)

One of the main conclusions of our previous work[10] was that the Raman spectra of the studied $SnO_2$:Ta transparent conductive oxide (exp.: 1.25 at% Ta, calc.: 1.04 at%) are to be understood as the superposition of Raman lines arising from three structural contributions, *i.e.*, $SnO_2$:Ta, $SnO_2$:Ta-$O_i$-far and $SnO_2$:Ta-$V_{Sn}$-far. The present investigation confirmed the co-existence of $V_{Sn}$- and $O_i$-type defects. A new result is the evident presence of a second $V_{Sn}$-type defect structure in the thin-film samples. Both the calculated Raman spectra of the $SnO_2$:Ta-$O_i$-far and $SnO_2$:Ta-$V_{Sn}$-near structures exhibit a line at a frequency close to the experimental frequency of the $D_2$ mode.[10] The main resonance Raman maximum of the $D_2$ line at 427 nm is related to the $O_i$-type defect. Its second excitation profile maximum at 513 nm is found at the same wavelength as the excitation profile maximum of the $D_1$-high line (515 nm) within the experimental accuracy and is assigned to the electronic resonance of the $V_{Sn}$-near defect structure. Thus, in contrast to the two other observed point defects, the $V_{Sn}$-near defect in $SnO_2$:Ta has two characteristic Raman lines that are enhanced under fulfilled resonance conditions. Notably, the co-existence of two $V_{Sn}$-type structures is in better agreement with our previous DFT stability calculations than the preference of the $V_{Sn}$-far defect, given that for the $V_{Sn}$-near defect the formation energy was found to be 1.4 eV smaller than for $V_{Sn}$-far (ref. 10, ESI).

The contribution of $SnO_2$:Ta domains without additional point defects was mainly concluded from the very good agreement between the measured (605 $cm^{-1}$) and calculated (593/601 $cm^{-1}$) frequencies of the $A_{1g}$-derived $L_4$ line.[10] The $L_5$ line was attributed to $SnO_2$:Ta with $O_i$-type defects (exp.: 625 $cm^{-1}$; calc.: 614 $cm^{-1}$). This defect has a line pair at 586/597 $cm^{-1}$ in the calculated Raman spectra. Its mean frequency deviation from the experimental $L_4$ frequency is 13.5 $cm^{-1}$ (−2.2%), compared to 8 $cm^{-1}$ (−1.3%) for $SnO_2$:Ta. This is also a very good agreement and allows the $L_4$ line to be assigned to $SnO_2$:Ta with $O_i$-type defects as well. The detailed comparison of the calculated $SnO_2$:Ta and $SnO_2$:Ta-$O_i$-far Raman spectra with the experimental spectrum shows a very similar structure, without characteristic lines safely pointing to the existence of defect-free $SnO_2$:Ta in the TTO samples under study (Fig. 7). For this comparison, the Raman spectrum recorded with 785 nm laser radiation was used, because the resonance enhancement effects are weak under this condition, and many lattice modes are better visible. The comparison displayed in Fig. 7 reveals

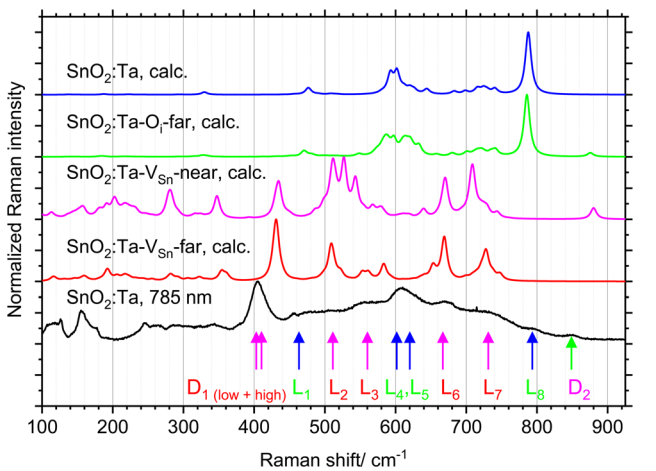


Fig. 7 Comparison of the experimental Raman spectrum of $SnO_2$:Ta measured at 785 nm laser radiation with the calculated Raman spectra of $SnO_2$:Ta-$V_{Sn}$-far, $SnO_2$:Ta-$V_{Sn}$-near, $SnO_2$:Ta-$O_i$-far, and $SnO_2$:Ta. The spectra were normalized and shifted along the *y*-axis for clarity. The label D denotes defect modes, and the label L denotes lattice modes. The colour code connects the lines in the experimental spectrum with the corresponding modes in the calculated Raman spectra. The calculated spectra were obtained in our previous work.[10]

a predominantly group-like correlation of the experimental and calculated Raman lines. The first group includes the experimental $D_1$ ($D_1$-low and $D_1$-high), $L_2$, $L_3$, $L_6$, and $L_7$ lines, which have close correspondence to the calculated spectra of $SnO_2$:Ta with $V_{Sn}$-far and $V_{Sn}$-near defects. This is indicated by the red/pink colour code in Fig. 7. The existence of both types of defects was concluded from the splitting of the $D_1$ line and the slightly different Raman excitation profile maxima. The second group includes the $L_1$, $L_4$, $L_5$, and $L_8$ lines, which have corresponding lines in the calculated spectra of $SnO_2$:Ta and $SnO_2$:Ta-$O_i$-far (Fig. 7, green/blue colour code). While the presence of the latter is evident due to the presence of the $D_2$ line, its excitation profile maximum at 427 nm, and the corresponding VB splitting found in the DFT calculations, there is no compelling reason to assume the existence of defect-free $SnO_2$:Ta domains in the studied TTO samples.

Based on the identification of three defect structures in the studied $SnO_2$:Ta thin films, it seems worth giving a more detailed description of the normal modes, which are responsible for the characteristic $D_1$, $D_2$, $L_4$, and $L_5$ Raman lines. The $D_1$ defect line of both $SnO_2$:Ta-$V_{Sn}$-far and $SnO_2$:Ta-$V_{Sn}$-near is caused by the O atom vibrations of dangling Sn–O bonds in the direct vicinity of the tin vacancy. The $D_2$ mode of $SnO_2$:Ta-$O_i$-far arises from the stretching vibration of an $O_2$ dimer with an O–O bond distance of 151 pm embedded in the crystal structure of $SnO_2$:Ta. In the case of the $SnO_2$:Ta-$V_{Sn}$-near defect structure, a stretching vibration of the oxygen atoms in the distorted $TaO_6$ octahedron next to the $V_{Sn}$ defect has almost the same frequency. The calculated frequencies of both $D_2$ modes are almost the same, *i.e.*, 875 $cm^{-1}$ and 880 $cm^{-1}$. Their simultaneous presence in the spectra could only by revealed by measuring their excitation profiles. In contrast to the localized $D_1$ and $D_2$ modes, the lattice modes responsible for the $A_{1g}$-derived lines $L_4$ + $L_5$ are delocalized over the whole supercell, and consequently the whole crystal lattice. Unlike in the $SnO_2$:Ta thin films investigated here, the Raman spectra of $SnO_2$ nanocrystal samples with diameters from 3 nm to 10 nm are dominated by a line at approx. 570 $cm^{-1}$, which is attributed to near-surface oxygen vacancy defects.[57] In SI 5,† we included the coordinates of several frames (as *.xyz files) of the six most relevant vibrational modes responsible for the characteristic Raman lines (*i.e.*, $D_1$, $D_2$, $L_4$ and $L_5$) in the different model structures of this study. These files allow the direct visualization of each normal mode using standard software such as Jmol or Avogadro.

### 4.2 Electronic structure of $SnO_2$:Ta (1.25 at% Ta)

The combination of Raman spectroscopic, optical, and hybrid functional DFT data in this study allowed detailed conclusions about the electronic structure of Ta-doped $SnO_2$ (1.25 at% Ta). The studied thin film samples, which are slightly O-rich, exhibit two $V_{Sn}$- and one $O_i$-type defects, in addition to the substitutional Ta atom, $Ta_{Sn}$. These additional point defects have a significant effect on the electronic structure of the material. This is predominantly expressed in the broadening and splitting of the electronic states at the top of the valence band, and specifically in an upshift of the upper VB states relative to the DOS maximum of the valence band. The upshift is highest for the $V_{Sn}$-type defect located far from the $Ta_{Sn}$ atom, and smallest for the $O_i$-far-type defect, the chemical nature of which is a diatomic peroxide molecule ion. The ordering of the VBM upshift correlates with the calculated degree of structural deformation of the lattice and the ordering of the defect formation energies published previously (ESI in ref. 10). The defect-induced VBM states are the initial states for the electronic transitions, which were identified by the Raman excitation profiles of the characteristic defect lines. Depending on the specific point defect, different transition energies were found. In detail, we obtained the following correlations between the experimental Raman and the hybrid functional DFT data for the individual point defects (Table 5).

Moreover, the following characteristics of the defects were found:

(1) The $V_{Sn}$-far type defect has a delocalized nature and causes the strongest perturbation of the VB electronic structure with at least three additional features at its high-energy edge.

(2) The second $V_{Sn}$-type defect, $V_{Sn}$-near, where the tin vacancy directly neighbours the $Ta_{Sn}$ atom, also produces significant perturbations of the electronic structure with at least two additional VB-DOS features compared to $SnO_2$:Ta.

(3) The $O_i$-far defect has a strongly localized nature. It is responsible for three narrow DOS states, one of them resulting in an additional, up-shifted VBM peak. The overall perturbation of the DOS is smaller than for the two $V_{Sn}$-type defects.

The major optical absorption of $SnO_2$:Ta (1.25 at% Ta) at 4.13 ± 0.10 eV is due to a dipole-allowed direct inter-band transition, which is assigned to the fundamental band-gap transition of the studied TCO. Fig. 8 shows a schematic illustration of the electronic band structure of Ta-doped $SnO_2$ (1.25 at% Ta) and the measured electronic transitions. This figure considers the localized or delocalized origin of the three defect states, and also the relative position and localized nature of the Ta 5d states in the conduction band (see Section 3.4). The relative transition energies, reflected by the length of the arrows, correspond to the values obtained by the Raman excitation profiles and optical spectra. The relative energies of the defect states were chosen to fit with the experimental transition

Table 5 Characteristic Raman signatures and electronic properties of the three identified point defects in $SnO_2$:Ta (1.25 at% Ta)

| Defect type | Characteristic Raman lines and Raman shifts | Electronic transition energy | Valence band splitting ($\Delta E_s$) |
|---|---|---|---|
| $V_{Sn}$-far | $D_1$-low: 402 ± 1 $cm^{-1}$ | 2.33 eV | 1.44 eV |
| $V_{Sn}$-near | $D_1$-high: 412 ± 1 $cm^{-1}$ + $D_2$: 848 ± 1 $cm^{-1}$ | 2.41 … 2.42 eV | 1.16 eV |
| $O_i$-far | $D_2$: 848 ± 1 $cm^{-1}$ | 2.90 eV | 1.03 eV |

 

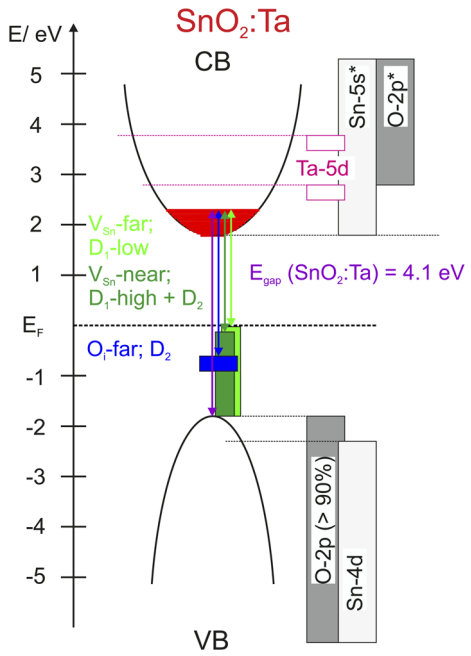


Fig. 8 Schematic of the obtained electronic band structure of Ta-doped $SnO_2$ (1.25 at% Ta) and the electronic transitions identified in this study.

energies, *i.e.* they are slightly shifted towards the bandgap centre compared to the splitting energies obtained in the DFT calculations.

## 5 Conclusions

Detailed insight in the electronic structure of the $SnO_2$:Ta transparent conductive oxide (1.25 at% Ta) was achieved by the combination of resonance Raman spectroscopy, optical spectroscopy, and hybrid functional DFT calculations. Ta was confirmed to be an effective donor for $SnO_2$ due to the favourable location of the Ta 5d states at approx. 1 eV above the CBM. The electronic transition energies of additional point defect states were obtained from the Raman excitation profile maxima. Two Sn-vacancy type point defects and one O-interstitial type defect could be distinguished. The DFT calculations revealed significant changes in the valence band electronic structure due to $O_i$- and $V_{Sn}$-type point defects, visible by VB splitting with additional states at the top of the valence band compared to defect-free $SnO_2$ and $SnO_2$:Ta. The observed VB splitting shows the reverse order to the electronic transition energies of the defect states. This finding has fundamental importance for the conclusions of this work. The results reveal the significantly larger distortion of the electronic structure due to $V_{Sn}$-type defects than due to $O_i$-type defects. In addition, the distortion is larger when substitutional Ta and Sn vacancy have a large distance, and smaller if they are direct neighbours. These findings were explained by the localized nature of the $O_i$-type states and the delocalization of the $V_{Sn}$-type states over four O atoms located in close proximity to the tin vacancy. Regarding the question whether the $V_{Sn}$- and $O_i$-type defects are favourable or unfavourable for the electrical and optical properties of $SnO_2$:Ta, this work concluded that the latter is true. Their optical excitations in the visible range reduce the transmittance. However, these point defects are not the major limiting factor for the performance of the studied thin films. This was concluded from the significantly higher optical carrier mobility of $(35 \pm 3)$ $cm^2\ V^{-1}\ s^{-1}$ compared to the electric mobility of $(14 \pm 3)$ $cm^2\ V^{-1}\ s^{-1}$.[9] As the main factor for this difference, intergrain scattering of the charge carriers at grain boundaries was proposed, which predominantly reduces the macroscopic electrical properties.[58,59] The defects studied in our recent manuscript are of intragrain nature or local origin and affect both the macroscopic and microscopic electrical properties.

In summary, the methodological combination applied in this study was demonstrated to be a powerful approach to get detailed insight into the electronic structure of the Ta-doped $SnO_2$ transparent conductive oxide. Thus, it is tempting to apply it to other TCOs to determine whether this knowledge about the point defects can help to optimize their electric and optical properties.

## Data availability

Data for this article, including primary Raman, optical, and DFT data are available at Rodare repository of HZDR at **https://doi.org/10.14278/rodare.3293**.

## Author contributions

Matthias Krause: conceptualization, methodology, investigation, formal analysis, data curation, writing – original draft, writing – review & editing; Carlos Romero-Muñiz: investigation, data curation, formal analysis, visualization, writing – original draft, review & editing; Oleksandr Selyshchev: investigation, data curation, writing – original draft, review & editing; Dietrich R. T. Zahn: writing – review & editing; Ramon Escobar-Galindo: conceptualization, funding acquisition, project administration, writing – original draft, review & editing. The article was written without any assistance of artificial intelligence.

## Conflicts of interest

There are no conflicts to declare.

## Acknowledgements

Angela Schneider, Jens Zscharschuch, and Robert Aniol (all from HZDR) are gratefully acknowledged for technical assistance. For sample preparation, we thank Dr F. Lungwitz (HZDR) and M.Sc. A. Mendez (Nano4Energy S.L., Madrid, Spain). We thank Dr P. Zahn and Prof. A. Erbe (HZDR) for careful proofreading of the manuscript and helpful comments. C. R.-M. acknowledges financial support by the Ramón y Cajal program of the Spanish Ministry of Science and Innovation (Ref. RYC2021-031176-I). We also thank the computing time provided by the Servicio de Supercomputación de la Universidad de Granada in Albaicín supercomputer.

## References


1 K. L. Chopra, S. Major and D. K. Pandya, *Thin Solid Films*, 1983, **102**, 1–46.
2 M. Batzill and U. Diebold, *Prog. Surf. Sci.*, 2005, **79**, 47–154.
3 K. Ellmer, *Nat. Photonics*, 2012, **6**, 808–816.
4 S. C. Dixon, D. O. Scanlon, C. J. Carmalt and I. P. Parkin, *J. Mater. Chem. C*, 2016, **4**, 6946–6961.
5 K. Ellmer, R. Mientus and S. Seeger, Metallic Oxides (ITO, ZnO, $SnO_2$, $TiO_2$), in *Transparent Conductive Materials: Materials, Synthesis, Characterization, Applications*, ed. D. Levy and E. Castellon, Wiley-VCH Verlag GmbH & Co. KGaA, Weinheim, 2018, pp. 33–80, DOI: 10.1002/9783527804603.
6 G. K. Dalapati, H. Sharma, A. Guchhait, N. Chakrabarty, P. Bamola, Q. Liu, G. Saianand, A. M. S. Krishna, S. Mukhopadhyay, A. Dey, T. K. S. Wong, S. Zhuk, S. Ghosh, S. Chakrabortty, C. Mahata, S. Biring, A. Kumar, C. S. Ribeiro, S. Ramakrishna, A. K. Chakraborty, S. Krishnamurthy, P. Sonar and M. Sharma, *J. Mater. Chem. A*, 2021, **9**, 16621–16684.
7 H. Toyosaki, M. Kawasaki and Y. Tokura, *Appl. Phys. Lett.*, 2008, **93**, 132109.
8 M. Fukumoto, S. Nakao, K. Shigematsu, D. Ogawa, K. Morikawa, Y. Hirose and T. Hasegawa, *Sci. Rep.*, 2020, **10**, 6844.
9 F. Lungwitz, R. Escobar-Galindo, D. Janke, E. Schumann, R. Wenisch, S. Gemming and M. Krause, *Sol. Energy Mater. Sol. Cells*, 2019, **196**, 84–93.
10 M. Krause, M. Hoppe, C. Romero-Muñiz, A. Mendez, F. Munnik, A. Garcia-Valenzuela, C. Schimpf, D. Rafaja and R. Escobar-Galindo, *J. Mater. Chem. A*, 2023, **11**, 17686–17698.
11 K. Stöwe and M. Weber, *Z. Anorg. Allg. Chem.*, 2020, **646**, 1470–1480.
12 R. K. Gupta, K. Ghosh, S. R. Mishra and P. K. Kahol, *Appl. Surf. Sci.*, 2008, **254**, 4018–4023.
13 E. Terzini, P. Thilakan and C. Minarini, *Mater. Sci. Eng., B*, 2000, **77**, 110–114.
14 M. Weidner, J. J. Jia, Y. Shigesato and A. Klein, *Phys. Status Solidi B*, 2016, **253**, 923–928.
15 R. Ramarajan, J. M. Fernandes, M. Kovendhan, G. Dasi, N. P. Reddy, K. Thangaraju and D. P. Joseph, *J. Alloys Compd.*, 2022, **897**, 163159.
16 V. Uwihoreye, Z. N. Yang, J. Y. Zhang, Y. M. Lin, X. Liang, L. Yang and K. H. L. Zhang, *Sci. China Mater.*, 2023, **66**, 264–271.
17 H. Kim, R. C. Y. Auyeung and A. Piqué, *Thin Solid Films*, 2008, **516**, 5052–5056.
18 Z. Y. Banyamin, P. J. Kelly, G. West and J. Boardman, *Coatings*, 2014, **4**, 732–746.
19 B. Bissig, T. Jäger, L. Ding, A. N. Tiwari and Y. E. Romanyuk, *APL Mater.*, 2015, **3**, 062802.
20 Q. Shen, P. Yang, N. Li, M. J. Li, F. Chen and L. M. Zhang, *J. Wuhan Univ. Technol., Mater. Sci. Ed.*, 2016, **31**, 20–26.
21 L. S. Parshina, O. A. Novodvorsky, O. D. Khramova, I. A. Petukhov, V. A. Mikhalevsky, A. A. Lotin, E. A. Cherebilo and V. Y. Panchenko, *Opt. Quantum Electron.*, 2016, **48**, 316.
22 E. Shanthi, V. Dutta, A. Banerjee and K. L. Chopra, *J. Appl. Phys.*, 1980, **51**, 6243–6251.
23 B. Stjerna, E. Olsson and C. G. Granqvist, *J. Appl. Phys.*, 1994, **76**, 3797–3817.
24 C. Kilic and A. Zunger, *Phys. Rev. Lett.*, 2002, **88**, 095501.
25 A. K. Singh, A. Janotti, M. Scheffler and C. G. Van de Walle, *Phys. Rev. Lett.*, 2008, **101**, 055502.
26 K. G. Godinho, A. Walsh and G. W. Watson, *J. Phys. Chem. C*, 2009, **113**, 439–448.
27 J. Y. Wang, J. Y. Chang, S. X. Kang, Y. Chen and S. W. Fan, *Mater. Today Commun.*, 2023, **37**, 107632.
28 M. Behtash, P. H. Joo, S. Nazir and K. Yang, *J. Appl. Phys.*, 2015, **117**, 175101.
29 B. A. D. Williamson, T. J. Featherstone, S. S. Sathasivam, J. E. N. Swallow, H. Shiel, L. A. H. Jones, M. J. Smiles, A. Regoutz, T. L. Lee, X. M. Xia, C. Blackman, P. K. Thakur, C. J. Carmalt, I. P. Parkin, T. D. Veal and D. O. Scanlon, *Chem. Mater.*, 2020, **32**, 1964–1973.
30 P. P. Filippatos, N. Kelaidis, M. Vasilopoulou and A. Chroneos, *Sci. Rep.*, 2023, **13**, 20983.
31 J. F. Scott, *J. Chem. Phys.*, 1970, **53**, 852–853.
32 P. S. Peercy and B. Morosin, *Phys. Rev. B*, 1973, **7**, 2779–2786.
33 J. Zuo, C. Y. Xu, X. M. Liu, C. S. Wang, C. Y. Wang, Y. Hu and Y. T. Qian, *J. Appl. Phys.*, 1994, **75**, 1835–1836.
34 A. Dieguez, A. Romano-Rodriguez, A. Vila and J. R. Morante, *J. Appl. Phys.*, 2001, **90**, 1550–1557.
35 L. Z. Liu, T. H. Li, X. L. Wu, J. C. Shen and P. K. Chu, *J. Raman Spectrosc.*, 2012, **43**, 1423–1426.
36 J. X. Zhou, M. S. Zhang, J. M. Hong and Z. Yin, *Solid State Commun.*, 2006, **138**, 242–246.
37 F. Lungwitz, PhD thesis, Technische Universität Chemnitz, 2024.
38 A. Mendez, Master thesis, Universidad Politécnica de Madrid, 2018.
39 J. Tauc, R. Grigorovici and A. Vancu, *Phys. Status Solidi B*, 1966, **15**, 627–637.
40 A. R. Zanatta, *Sci. Rep.*, 2019, **9**, 11225.
41 A. V. Krukau, O. A. Vydrov, A. F. Izmaylov and G. E. Scuseria, *J. Chem. Phys.*, 2006, **125**, 224106.
42 G. Kresse and J. Furthmuller, *Phys. Rev. B:Condens. Matter Mater. Phys.*, 1996, **54**, 11169–11186.
43 P. Mori-Sánchez, A. J. Cohen and W. Yang, *Phys. Rev. Lett.*, 2008, **100**, 146401.
44 Q. Zhao and H. J. Kulik, *J. Chem. Theory Comput.*, 2018, **14**, 670–683.
45 J. B. Varley, A. Janotti and C. G. Van de Walle, *Phys. Rev. B:Condens. Matter Mater. Phys.*, 2010, **81**, 245216.
46 A. Jorio, M. S. Dresselhaus, R. Saito and G. F. Dresselhaus, *Raman Spectroscopy in Graphene Related Systems*, Wiley-VCH, Weinheim, 2012.
47 J. F. Scott, T. C. Damen, R. C. C. Leite and W. T. Silfvast, *Solid State Commun.*, 1969, **7**, 953–955.
48 M. A. Renucci, J. B. Renucci and M. Cardona, *Phys. Status Solidi B*, 1972, **49**, 625–631.


 

49 J. B. Renucci, W. Richter, M. Cardona and E. Schonherr, *Phys. Status Solidi B*, 1973, **60**, 299–308.
50 G. W. Rubloff, E. Anastassakis and F. H. Pollak, *Solid State Commun.*, 1973, **13**, 1755–1759.
51 W. Richter, R. Zeyher and M. Cardona, *Phys. Rev. B*, 1978, **18**, 4312–4324.
52 S. K. Doorn, D. A. Heller, P. W. Barone, M. L. Usrey and M. S. Strano, *Appl. Phys. A:Mater. Sci. Process.*, 2004, **78**, 1147–1155.
53 H. Kuzmany, *Solid State Spectroscopy – An Introduction*, Springer, Berlin, Heidelberg, New york, 1998.
54 R. Saito, M. Hofmann, G. Dresselhaus, A. Jorio and M. S. Dresselhaus, *Adv. Phys.*, 2011, **60**, 413–550.
55 A. R. Zanatta, *Sci. Rep.*, 2019, **9**, 11225.
56 D. J. Cheng, M. M. Zhang, J. F. Chen, C. X. Yang, X. F. Zeng and D. P. Cao, *J. Phys. Chem. C*, 2014, **118**, 2037–2043.
57 L. Z. Liu, X. L. Wu, F. Gao, J. C. Chen, T. H. Li and P. K. Chu, *Solid State Commun.*, 2011, **151**, 811.
58 D. H. Zhang and H. L. Ma, *Appl. Phys. A*, 1996, **62**, 487–492.
59 J. Steinhauser, S. Fay, N. Oliveira, E. Vallat-Sauvain and C. Ballif, *Appl. Phys. Lett.*, 2007, **90**, 142107.